

Nuclear structure within the relativistic mean field approach including chiral symmetry and quark confinement effects

M. Chamseddine,^{1,*} J.-P. Ebran,^{2,3} E. Khan,^{1,4} B. K. Pradhan,⁵ J. Margueron,⁶ H. Hansen,⁵ and G. Chanfray⁵

¹*IJCLab, Université Paris-Saclay, CNRS/IN2P3, 91405 Orsay Cedex, France*

²*CEA, DAM, DIF, F-91297 Arpajon, France*

³*Université Paris-Saclay, CEA, Laboratoire Matière en Conditions Extrêmes, 91680, Bruyères-le-Châtel, France*

⁴*Institut Universitaire de France (IUF)*

⁵*Institut de Physique des 2 Infinis de Lyon, CNRS/IN2P3, Université de Lyon, Université Claude Bernard Lyon 1, F-69622 Villeurbanne Cedex, France*

⁶*International Research Laboratory on Nuclear Physics and Astrophysics, Michigan State University and CNRS, East Lansing, MI 48824, USA*

The relativistic mean field approach, within a theoretical framework known as the chiral confining model, that incorporates both chiral symmetry breaking and quark confinement effects, is applied for the first time to study the properties of some spherical nuclei, such as binding energies and charge radii. The model parameters are calibrated using a Bayesian approach to reproduce nuclear empirical properties and global properties of doubly magic nuclei. For intermediate mass and heavy closed-shell nuclei, this model provides a satisfactory description of binding energies and charge radii, with standard deviations comparable to usual relativistic mean field models, while larger discrepancies are observed in light nuclei. This behavior is traced back to the constrained form of the chiral potential, which reduces flexibility away from saturation density and affects systems probing a broader density range, i.e., light nuclei. Charge radii are reproduced with excellent accuracy across all mass regions considered, although the corresponding density profiles remain slightly more diffuse than the experimental ones. Extending the analysis to open-shell nuclei using a separable Gogny pairing interaction reveals an enhanced pairing effect in this framework, which can lead to anomalous pairings even in closed shells. This is associated with the large Dirac effective mass, which reduces spin-orbit splittings and increases the density of single-particle states around the Fermi surface. A modest reduction of the pairing strength suppresses this anomaly at the diagnostic level, indicating that the pairing channel remains sensitive to the underlying single-particle structure generated by the model. Finally, we qualitatively explore departures from the linear sigma model potential, motivated by the Nambu–Jona-Lasinio framework, to understand the role of the chiral potential for finite nuclei properties. Allowing for variations of the cubic and quartic terms in the potential leads to improved results for light nuclei, and a reduction of the Dirac mass, which in turn suppresses the anomalous pairing. These results confirm the sensitivity of light nuclei to the global trend of the chiral potential, and the impact of the latter on the Dirac mass and thus the single-particle structure.

I. INTRODUCTION

The study of nuclear systems, from finite nuclei (FN) to nuclear matter, remains one of the most challenging problems in physics. It requires state-of-the-art many-body methods together with a proper understanding of the strong interaction in the relevant density and energy regimes. The nuclear interaction emerges as the residual low-energy manifestation of the strong interaction in its non-perturbative regime. While Quantum Chromodynamics (QCD) describes interactions between quarks and gluons, nuclear structure models are commonly formulated in terms of effective interactions between nucleons. This non-perturbative regime manifests itself through highly non-linear phenomena, such as spontaneous chiral symmetry breaking, which endows the QCD vacuum with a non-trivial structure, as well as color confinement.

Unlike QED, where the main difficulty lies in the many-body problem since the interaction is simple and perturbative over a wide range of energies, the low-energy regime relevant for nuclear physics requires the use of effective approaches. These include QCD-inspired phenomenological models at the quark level, such as the Nambu–Jona-Lasinio model (NJL) model [1], as well as systematically constructed effective theories based on the symmetries of QCD, such as Chiral Effective Field Theory (χ -EFT) [2]. For medium and heavy nuclei, where fully microscopic treatments remain computationally demanding, energy-density-functionals (EDF) approaches provide an efficient and accurate framework for global calculations. Within these EDFs, relativistic mean field (RMF) theory has been successful in describing

* mohamad.chamseddine@ijclab.in2p3.fr

nuclear structure. In addition, it is a covariant approach where spin, spin-orbit, or causality are automatically built-in in the formalism [3–5]. However, the Lagrangian used in the RMF approach remains phenomenological, with a weak or inexistent connection with the low-energy QCD regime.

In this work, we use the chiral confining model (CCM) framework, taken at the Hartree level, referred to as RMF-CC. RMF-CC is not an *ab initio* chiral-EFT construction; it is a QCD-motivated [6] effective covariant functional whose scalar sector is constrained by chiral symmetry. It additionally encodes confinement-inspired nucleon response through a scalar polarizability. It has been previously applied to describe nuclear matter properties [7–10]. This model is based on two main ideas: the identification of the nuclear physics σ meson, introduced in relativistic mean fields approaches, with the radial fluctuation of the chiral quark condensate, as proposed in Ref. [11], and the inclusion of a nucleon "polarization" effect induced by the nuclear environment, as in Refs. [6, 12, 13].

The paper is organized as follows: In Section II, we present the formalism framing the theoretical framework of our model. In Section III, we discuss the parameters of our model and the Bayesian procedure followed to calibrate these parameters. We then present our results in Section IV, where we discuss doubly magic and open-shell nuclei. In Section V, we perform a systematic study of the spin-orbit potential within the RMF-CC phase space, examining both the constraints imposed by NEPs and the mechanisms governing its magnitude. In Section VI, we explore approaches beyond the Linear Sigma Model (L σ M) and explore the consequences for finite nuclei properties. Our results are summarized, and we present our conclusions in Section VII.

II. FRAMEWORK

A. Relativistic mean field Lagrangians

Considering only the lightest u and d quarks and the flavor number $N_f = 2$, the chiral fields associated with the fluctuations of the quark condensate $\langle \bar{q}q \rangle$ resulting from chiral symmetry breaking are usually parameterized in terms of a SU(2) matrix M as:

$$M = \sigma + i\vec{\tau} \cdot \vec{\phi} \equiv SU, \quad (1)$$

with $S = s + f_\pi$ and $U = e^{i\vec{\tau} \cdot \vec{\pi}/f_\pi}$, $\vec{\tau}$ being the Pauli matrices in isospin space. The scalar field σ (S) and pseudo-scalar fields $\vec{\phi}$ ($\vec{\pi}$) written in Cartesian (polar) coordinates appear as the dynamical degrees of freedom. One may be tempted to identify the usual sigma meson of the Walecka model (let us call it σ_W from now on) with the scalar field σ in Cartesian coordinates. It is, however, forbidden by chiral constraints, and this point has been first addressed by Birse [14]: it would lead to the presence of terms of order m_π in the NN interaction, which is not allowed as discussed in detail in [13] (see also [15] for a more recent review).

In this study, we follow Ref. [11] and identify σ_W with the chiral invariant s ($= S - f_\pi$) field associated with the radial fluctuation of the chiral condensate around the chiral radius f_π , in polar coordinates. It formally consists of promoting the chiral invariant scalar field s and the pion field $\vec{\pi}$ appearing in the matrix M in Eq. (1) to effective degrees of freedom. This was originally formulated in the framework of the Linear Sigma Model (L σ M) [6, 7, 11, 16, 17], but an explicit construction using a bosonization technique of the chiral effective potential can be done within the NJL model [18] where the L σ M potential is recovered through a second order expansion in $S^2 - f_\pi^2$ of the constituent quark Dirac sea energy. The latest versions of this chiral potential from NJL are used in Refs. [10, 15, 19].

This proposal, which gives a plausible answer to the long standing problem of the chiral status of Walecka theories, also has the merit of respecting all the desired chiral constraints [14]. In particular, the correspondence $s \equiv \sigma_W$ generates a coupling of the scalar field to the derivatives of the pion field, as expected in the physical world. Hence, the radial mode decouples from low-energy pions whose dynamics is governed by chiral perturbation theory. A detailed discussion of this somewhat subtle topic is given in Refs. [11, 13, 20], and in the following, we employ the notation s for the scalar field to avoid confusion with the meson σ .

The relativistic Lagrangian can generically be written as the sum of a kinetic fermionic term and meson-nucleon term. The kinetic term is

$$\mathcal{L}_N = \bar{\psi} (i\gamma^\mu \partial_\mu - M_N(s)) \psi, \quad (2)$$

where the field ψ represents the nucleon spinor, and $M_N(s)$ is the polarised nucleon mass defined in (5). The mesonic degrees of freedom are the chiral-invariant scalar field s and the isoscalar/isovector vector fields ω and ρ , together

with the Coulomb field. The meson-nucleon Lagrangian density then is

$$\begin{aligned}
\mathcal{L}_m = & \frac{1}{2} \partial^\mu s \partial_\mu s - V_\chi(s) \\
& - g_\omega \omega_\mu \bar{\psi} \gamma^\mu \psi + \frac{1}{2} m_\omega^2 \omega^\mu \omega_\mu - \frac{1}{4} F^{\mu\nu} F_{\mu\nu} \\
& - g_\rho \rho_{a\mu} \bar{\psi} \gamma^\mu \tau_a \psi + g_\rho \frac{\kappa_\rho}{2M_N} \partial_\nu \rho_{a\mu} \bar{\psi} \sigma^{\mu\nu} \tau_a \psi \\
& + \frac{1}{2} m_\rho^2 \rho_{a\mu} \rho_a^\mu - \frac{1}{4} G_a^{\mu\nu} G_{a\mu\nu} \\
& - e A_\mu \bar{\psi} \gamma^\mu \frac{1}{2} (1 - \tau_3) \psi - \frac{1}{4} H^{\mu\nu} H_{\mu\nu} \\
& + \frac{g_A}{2f_\pi} \partial_\mu \varphi_{\pi a} \bar{\psi} \gamma^\mu \gamma^5 \tau_a \psi - \frac{1}{2} m_\pi^2 \varphi_{\pi a} \varphi_{\pi a} \\
& + \frac{1}{2} \partial^\mu \varphi_{\pi a} \partial_\mu \varphi_{\pi a}.
\end{aligned} \tag{3}$$

where the symbols have their usual meaning. We remind that $g_A = 1.25$ is the axial coupling constant and $f_\pi = 94$ MeV is the pion decay constant. We also note the nucleon- ρ tensor coupling $f_\rho = g_\rho \kappa_\rho$. The pion and tensor ρ interactions do not contribute at the Hartree level, and thus, they will be removed in the following.

The chiral potential $V_\chi(s)$ in the scalar field s has a typical Mexican hat shape for spontaneous symmetry breaking, where s measures the chiral symmetry breaking. We consider in this study the $L\sigma M$ expression:

$$\begin{aligned}
V_\chi(s) = & \frac{\lambda}{4} ((f_\pi + s)^2 - v^2)^2 - f_\pi m_\pi^2 s \\
\equiv & \frac{m_s^2}{2} s^2 + \frac{m_s^2 - m_\pi^2}{2f_\pi} s^3 + \frac{m_s^2 - m_\pi^2}{8f_\pi^2} s^4.
\end{aligned} \tag{4}$$

More details on this effective chiral potential can be found, for instance, in Ref [8] and in references therein.

In the presence of the nuclear scalar field, nucleons get polarized and their mass is modified according to:

$$M_N(s) = M_N + g_s s + \frac{1}{2} \kappa_{NS} \left(s^2 + \frac{s^3}{3f_\pi} \right). \tag{5}$$

The nucleon polarisability parameter κ_{NS} , incorporates the effect of the nucleon response, i.e., the central ingredient of the quark-meson coupling model (QMC) introduced in the original pioneering work of P. Guichon [12]. As in Ref. [6] the scalar field dependent susceptibility is expressed as:

$$\tilde{\kappa}_{NS}(\bar{s}) \equiv \frac{\partial^2 M_N(s)}{\partial s^2} \Big|_{s=\bar{s}} = \kappa_{NS} \left(1 + \frac{\bar{s}}{f_\pi} \right), \tag{6}$$

which vanishes at full chiral restoration, i.e., $\bar{s} = -f_\pi$, where \bar{s} is the value taken by the s field in the ground state. We usually work with the dimensionless parameter C_{NS} defined as,

$$C_{NS} \equiv \frac{\kappa_{NS} F_\pi^2}{2M_N}. \tag{7}$$

B. Field equations and Hamiltonian

In the mean field approximation, the mesons take their ground state expectation values: $s \mapsto \bar{s}$, $\omega^\mu \mapsto \bar{\omega}^0 \equiv \bar{\omega}$, $\rho_a^\mu \mapsto \bar{\rho}_3^0 \equiv \bar{\rho}$, $A^\mu \mapsto \bar{A}^0 \equiv \bar{A}$. We can now list the equations of motion of the different contributing meson fields:

$$\begin{aligned}
-\nabla^2 \bar{s}(\mathbf{r}) + V'_\chi(\bar{s}) &= - \frac{dM_N(s)}{ds} \Big|_{\bar{s}} \langle \bar{\Psi} \Psi \rangle(\mathbf{r}) = -g_s^*(\bar{s}) \langle \bar{\Psi} \Psi \rangle(\mathbf{r}) \\
-\nabla^2 \bar{\omega}(\mathbf{r}) + m_\omega^2 \bar{\omega}(\mathbf{r}) &= g_\omega \langle \Psi^\dagger \Psi \rangle(\mathbf{r}) \\
-\nabla^2 \bar{\rho}(\mathbf{r}) + m_\rho^2 \bar{\rho}(\mathbf{r}) &= g_\rho \langle \Psi^\dagger \tau_3 \Psi \rangle(\mathbf{r}), \\
-\nabla^2 \bar{A}(\mathbf{r}) &= e \left\langle \Psi^\dagger \frac{1 - \tau_3}{2} \Psi \right\rangle(\mathbf{r})
\end{aligned} \tag{8}$$

where we define the following quantities:

$$\begin{aligned}
\langle \bar{\Psi} \Psi \rangle(\mathbf{r}) &= \rho_s(\mathbf{r}) = \rho_{s,p}(\mathbf{r}) + \rho_{s,n}(\mathbf{r}) , \\
\langle \Psi^\dagger \Psi \rangle(\mathbf{r}) &= \rho_b(\mathbf{r}) = \rho_{b,p}(\mathbf{r}) + \rho_{b,n}(\mathbf{r}) , \\
\langle \Psi^\dagger \tau_3 \Psi \rangle(\mathbf{r}) &= \rho_b^{(3)} = \rho_{b,n}(\mathbf{r}) - \rho_{b,p}(\mathbf{r}) , \\
\left\langle \Psi^\dagger \frac{1 - \tau_3}{2} \Psi \right\rangle(\mathbf{r}) &= \rho_c(\mathbf{r}) ,
\end{aligned} \tag{9}$$

where p/n stands for protons/neutrons and $\tau_3(n/p) = +1/-1$ respectively.

The EoM for the nucleon can be written as:

$$[-i\gamma^\mu \partial_\mu + (M_N + \Sigma_S(\mathbf{r})) + \gamma_0 \Sigma^0(\mathbf{r})] \psi(\mathbf{r}) = 0 , \tag{10}$$

with the scalar and time-like component potentials defined as:

$$\Sigma_S(\mathbf{r}) = M_N(\bar{s}) - M_N , \tag{11}$$

$$\Sigma_0(\mathbf{r}) = g_\omega \bar{\omega}(\mathbf{r}) + g_\rho \tau_3 \bar{\rho}(\mathbf{r}) + \frac{1}{2} e(1 - \tau_3) \bar{A}(\mathbf{r}) . \tag{12}$$

We can finally define the hamiltonian density

$$\begin{aligned}
\mathcal{H}(\mathbf{r}) &= \bar{\Psi}(-i\gamma^i \partial_i + M_N)\Psi + \left(M_N(\bar{s}) - M_N \right) \rho_s(\mathbf{r}) + V_\chi(\bar{s}) - \frac{1}{2} \bar{s} V_\chi'(\bar{s}) - \frac{1}{2} \bar{s} g_s^*(\bar{s}) \rho_s(\mathbf{r}) \\
&+ \frac{1}{2} \left(g_\omega \bar{\omega} \rho_b(\mathbf{r}) + g_\rho \bar{\rho} \rho_b^{(3)}(\mathbf{r}) + e \bar{A} \rho_c(\mathbf{r}) \right) ,
\end{aligned} \tag{13}$$

and the total energy E is obtained as: $E = \int d\mathbf{r} \mathcal{H}(\mathbf{r})$.

III. PARAMETRIZATION AND FITTING PROCEDURE

In this study, we will employ a Bayesian approach using the Markov Chain Monte-Carlo (MCMC) method. In this way, the full exploration of the uncertainties in the experimental data is translated into uncertainties in the free parameters of the model and in other predicted quantities that we will see in the results.

In the Bayesian approach, the so-called "data" refer to experimental data, e.g., binding energies B , charge radii R_c , and pseudo-data such as the nuclear empirical parameters (NEPs): the saturation density n_{sat} , saturation energy E_{sat} , symmetry energy E_{sym} , and the incompressibility modulus K_{sat} (see Refs. [21, 22] for more details). A certain "parameterization" of the model refers to the model's parameters, i.e., quantities like coupling constants, e.g., g_ω , g_s , and C_{NS} , or masses, e.g., m_s , which directly enter into the definition of the model. A "parameterization" can therefore be simply represented by the set $\{\theta_i\}$ of these parameters. They will be fixed in such a way as to reproduce the previously mentioned "data". The Bayesian probability associated with a certain parameterization and a set of data can be obtained in two different ways, since (Bayes theorem):

$$P(\{\theta_i\} | \text{data}) \times P(\text{data}) = P(\text{data} | \{\theta_i\}) \times P(\{\theta_i\}) , \tag{14}$$

where $P(\{\theta_i\} | \text{data})$ is the posterior probability associated with a parameterization given a set of "data", $P(\text{data})$ is the evidence, which is defined as the normalization of the posterior probability. We have $P(\text{data} | \{\theta_i\})$, the likelihood probability associated with a set of "data" given a parameterization, which can be expressed, for instance, as

$$\log P(\text{data} | \{\theta_i\}) = -\frac{1}{2} \frac{1}{N_{\text{dof}}} \sum_i \frac{[O_i(\text{data}) - O_i(\{\theta_i\})]^2}{\Delta O_i^2} , \tag{15}$$

where N_{dof} is the number of independent "data" – the number of "data" minus the number of parameters – and the sum goes over the number of data indexed by i , where $O_i(\text{data})$ represents a measured data and $O_i(\{\theta_i\})$ its prediction from the model. ΔO_i^2 is related to the uncertainty in the data originating from the measurement, but it can also incorporate the uncertainty of the model [23]. Finally, the probability $P(\{\theta_i\})$ in Eq. (14) is the prior probability, which represents the *a-priori* knowledge on the model parameters.

The Bayesian framework allows us to investigate the propagation of experimental uncertainties on i) our model's parameters as well as on ii) our predictions. By marginalizing over all other parameters, one could generate a Probability Distribution Function (PDF) associated to the model parameters and to our predictions.

TABLE I. Model parameters (masses and coupling constants) fixed in the present analysis.

M_N	m_ω	m_ρ	m_π	f_π
MeV	MeV	MeV	MeV	MeV
938.9	783.0	779.0	139.6	94.0

TABLE II. The NEPs (centroids and standard deviations), taken from [21], which are imposed by adjusting the variable model parameters m_s , g_s , C_{NS} , g_ω and g_ρ :

NEP	centroid	std. dev.
E_{sat} (MeV)	-15.8	0.3
n_{sat} (fm^{-3})	0.155	0.005
E_{sym} (MeV)	32	2
K_{sat} (MeV)	230	20

The fixed parameters of this model are given in Table I. At the Hartree level, the contributions are governed by the ratio (g_i/m_i) for the quadratic interactions (as is the case for $i = \omega, \rho$ interactions), so we simply fix the masses to the bare ones and keep only the coupling constants as variables. The code used for finite nuclei computations is from [24], adapted to our current model.

The variable model parameters are m_s , g_s , C_{NS} , g_ω and g_ρ . They are fitted to reproduce the NEPs given in Table II, as well as the binding energies and the charge radii measured for the doubly magic nuclei given in Table III.

The uncertainties considered in the likelihood probability (15) are now detailed. We consider the following uncertainty for the binding energy [27]

$$\Delta_B = 2.0 \text{ MeV}.$$

The charge radius is defined via the known empirical formula [28]

$$R_c^2 = R_p^2 + 0.64 \text{ fm}^2, \quad (16)$$

where R_p denotes the root mean square (rms) radius of the proton density distribution and the term 0.64 fm^2 approximately accounts for the finite size of the proton and the contribution of the spin-orbit and the neutron to the charge radius [24]. We consider the following uncertainty for the charge radius [27]

$$\Delta_{R_c} = 0.1A^{-1/3} \text{ fm}.$$

No priors are imposed on the parameters, except that they are positive (to reduce the parameter space to be explored to only physical values).

Finally, we consider the best model corresponding to the parameter set for which the posterior probability is maximal, and we refer to it as RMF-CC1 from now on.

TABLE III. Binding energies and available charge radii measurements of the seven doubly magic nuclei considered for the fit. The experimental error bars are given in parenthesis, and (-) stands for experimental error-bars smaller than the number of digits shown in the table.

Z	N	nucleus	B (MeV) Ref. [25]	R_c (fm) Ref. [26]
8	8	^{16}O	-127.6193(-)	2.6991(52)
20	20	^{40}Ca	-342.0521(-)	3.4776(19)
20	28	^{48}Ca	-416.0009(1)	3.4771(20)
28	28	^{56}Ni	-483.9956(4)	-
50	50	^{100}Sn	-825.2944(3000)	-
50	82	^{132}Sn	-1102.8430(20)	4.7093(76)
82	126	^{208}Pb	-1636.4301(11)	5.5012(13)

IV. RESULTS

In the following, we present and discuss our results: we start with doubly magic nuclei, and then we consider open-shell nuclei.

A. Doubly magic nuclei

After performing the fitting procedure discussed in the previous section, we are now ready to analyze the obtained results. Figure 1 displays the PDFs for the model parameters and the NEPs, which allows us to extract the model uncertainty, defined as the 68% credible interval (CI) of the distributions. We thus obtain the lower and upper bounds $\sigma_{\text{model}}^{\pm}$. The resulting optimal parameters (maximizing the posterior) obtained from the fitting, referred to as RMF-CC1, are shown in Table IV, where we have also shown the parametrization from the well-known non-linear scalar interaction model NL3 [29] and the density dependent DD-ME2 [30]. We additionally consider the Parity Doublet Model (PDM), applied to finite nuclei in Ref. [31] for 2 reasons: it also employs a chiral potential similar to our model, however they go to higher orders in the field (up to 6th order) with extra free parameters. The second reason is that the nucleon mass also depends on the scalar field, but the origin of this dependence is from the chiral partner of the nucleon, $N^*(1535)$, and not from confinement effects as in RMF-CC. In the following we consider the parameter set 3 of their paper, named PDM-3. This model turns out to be an important one once we discuss pairing in Section IV B.

The NL3 model shares several similarities with RMF-CC one, since both contain a non-linear scalar interaction. However, while the cubic and quartic coefficients are fixed by chiral symmetry in RMF-CC, see Sec. II, these coefficients are treated as free parameters in NL3. Additionally, the nucleon polarization in both NL3 and DD-ME2 is not considered, which can be reproduced in the RMF-CC approach by setting $C_{\text{NS}} = 0$. For a detailed comparison between RMF-CC and NL3, see Ref. [8].

The first quantities of interest are structure properties, mainly the binding energies and the charge radii. Note that this is the first application of the RMF-CC approach to finite nuclei and we would like to check whether our parametrization was able to correctly predict these nuclear structure properties, all the while respecting NEP constraints. Table V shows the reproduced NEPs obtained for different models. We first notice the symmetry energy, which is larger than the experimental value by about 20%. The posterior favors a rather stiff symmetry energy despite the nominal data constraint. This indicates a residual tension in the isovector channel of the present density-independent RMF-CC1, similar to what is observed in stiff nonlinear RMF parameterizations such as NL3. This suggests that a density-dependent isovector coupling, or an additional isovector degree of freedom, may be required for a quantitatively accurate isovector sector, as is the case for DD-ME2 for example.

Table V also displays two "effective masses", the Dirac mass, which appears in the Dirac equation (10) as

$$M_D^* = M_N + \Sigma_S, \quad (17)$$

known to be related to the spin-orbit potential strength, and the non-relativistic (NR) mass, M_{NR}^* , known to influence the density of single particle states. The latter can be extracted from the NR reduction of the Dirac equation into a Schrodinger-equivalent equation (see Ref. [9]), and is defined for nuclear matter at the Hartree level as:

$$M_{NR}^* = M_N - \Sigma_0. \quad (18)$$

It should be noted that these 2 masses are governed by different mesons, where M_D^* is controlled by the scalar field s while M_{NR}^* by the vector fields ω and ρ . For more details on the different conventions on effective masses, see

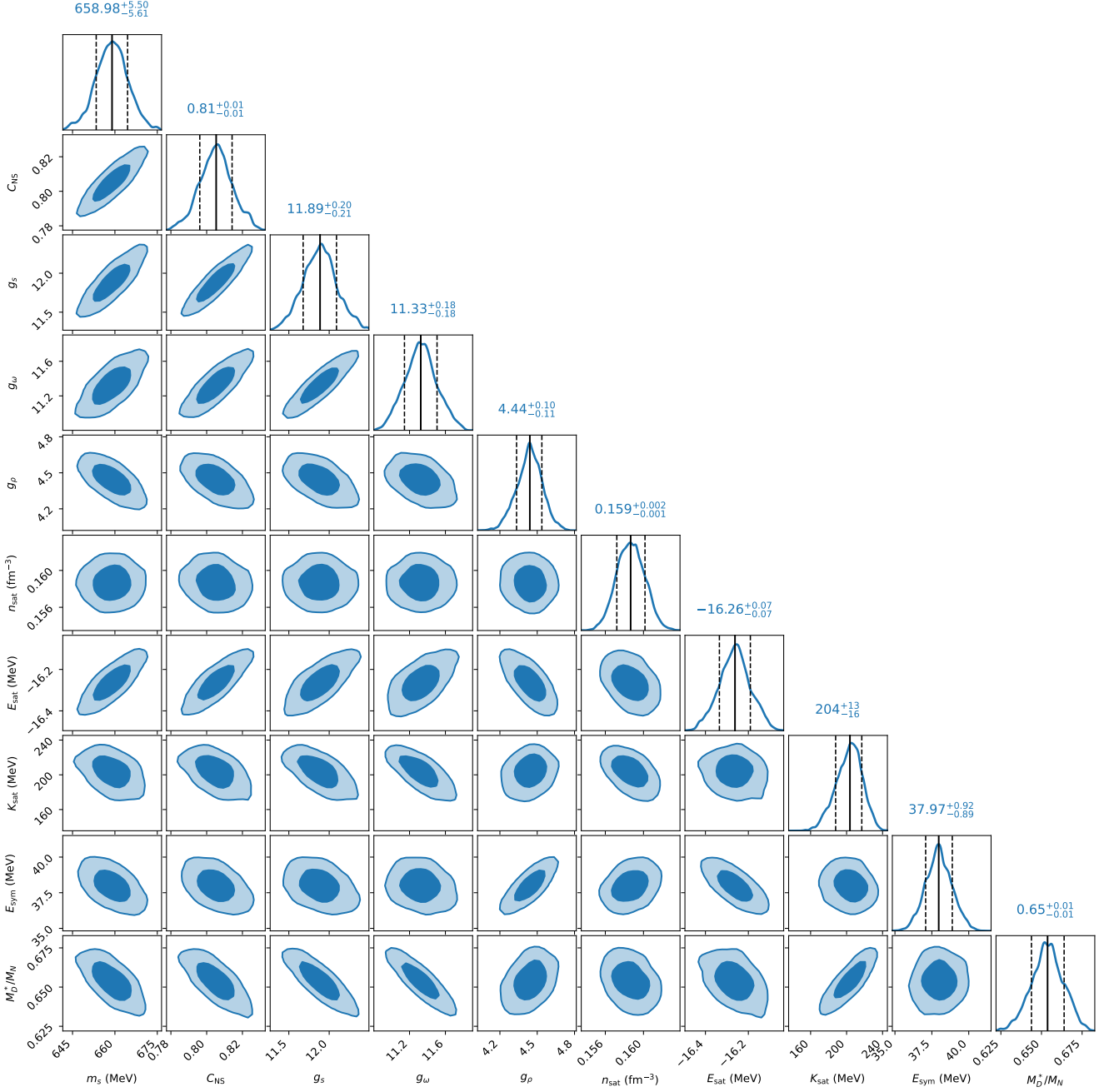


FIG. 1. Corner plot showing the joint (off-diagonal panels) and marginalized (diagonal panels) posterior distributions for the parameters (m_s in MeV, C_{NS} , g_s , g_ω , g_ρ) and the NEPs: n_{sat} (fm^{-3}), E_{sat} , K_{sat} , E_{sym} in MeV, and the Dirac mass M_D^*/M_N of the RMF-CC1 model fitted to the data of Tables II and III.

Refs. [32–34]. Note that the Dirac and NR masses are larger for both RMF-CC1 and PDM-3 compared to NL3 and DD-ME2.

The binding energies per nucleon and the charge radii of the nuclei employed in the fit are shown in Figs. 2 and 3. The error bars are defined as $\sigma^\pm = \sqrt{\sigma_{\text{model}}^{\pm 2} + \sigma_{\text{exp}}^2}$. For the binding energy, we observe a bigger deviation from experiments for the light nuclei, especially ^{16}O and ^{40}Ca . In contrast, NL3 and DD-ME2 provide more flexibility through either free parameters in the non-linear scalar potential or density-dependent couplings, and are fitted to both light and heavy nuclei. In the RMF-CC model, the scalar potential is constrained by chiral symmetry, which is mainly calibrated through bulk properties. To see this, we plot the profile of $\bar{s}(r)$ and $\bar{\omega}(r)$ in Figure 4, for both ^{16}O and ^{208}Pb , in RMF-CC1 and NL3, since they both exhibit non-linear scalar interactions. We observe no large qualitative

TABLE IV. Model parameters maximizing the posterior probability for the FN data and the NEPs (RMF-CC1). The quoted uncertainties correspond to 68% credible intervals from the Bayesian posterior distribution. We additionally show the NL3 [29], DD-ME2 [30] and PDM-3 [31] models for comparison. The (-) indicates parameters undefined for the specific model, and the details of the parameterization can be found in [31].

Parameter	RMF-CC1	NL3	DD-ME2	PDM-3
m_s (MeV)	$659.474^{+5.496}_{-5.605}$	508.194	550.124	382.140
g_s	$11.927^{+0.204}_{-0.210}$	10.217	10.5396	-
g_ω	$11.373^{+0.182}_{-0.182}$	12.868	13.0189	7.036
g_ρ	$4.430^{+0.097}_{-0.107}$	4.474	3.6836	3.958
C_{NS}	$0.8064^{+0.0089}_{-0.0092}$	0	0	-

TABLE V. The reproduced NEPs using the parametrization of Table IV, with the uncertainties corresponding to the 68% credible intervals from the Bayesian posterior distribution, compared to the NL3 [29], DD-ME2 [30] and PDM-3 [31] predictions.

Parameters	RMF-CC1	NL3	DD-ME2	PDM-3
E_{sat} (MeV)	$-16.26^{+0.07}_{-0.07}$	-16.30	-16.14	-16.22
n_{sat} (fm $^{-3}$)	$0.159^{+0.002}_{-0.001}$	0.1483	0.152	0.16
E_{sym} (MeV)	38^{+1}_{-1}	37.4	32.30	30.85
K_{sat} (MeV)	199^{+13}_{-16}	272	251	215
M_D^*/M_N	$0.65^{+0.01}_{-0.01}$	0.60	0.57	0.83
M_{NR}^*/M_N	$0.72^{+0.01}_{-0.01}$	0.67	0.65	0.89

differences in the field profiles, suggesting that the difference is not primarily due to the gradient terms associated with the meson fields themselves, but rather to the different functional dependence of the scalar contribution, in particular through the chiral potential and the nucleon polarization. The question we want to answer is why this difference plays a role for light nuclei and not heavy ones. For heavy nuclei, we have a large plateau for \bar{s} , so the field remains nearly constant throughout the nucleus before quickly dropping toward zero at the surface. This means that the potential is mainly probed locally around this value $\bar{s} \approx -35$ MeV, and since both models are fitted to saturation properties, their potentials behave similarly locally. In contrast, light nuclei do not exhibit such a plateau, and therefore probe a broader region of the potential, and as we move away from saturation, the two potentials differ significantly (the cubic and quartic terms even carry opposite signs in RMF-CC1 and NL3, this is discussed in [8]). Since NL3 has free parameters in the scalar potential, it can more easily accommodate the properties of light nuclei than the RMF-CC1 potential, which remains strongly constrained by chiral symmetry.

Another possible source of this difference in density-dependence is the absence of explicit Fock terms. Missing exchange contributions are effectively absorbed into the fitted Hartree couplings around the calibration domain. Away from saturation, and especially in light nuclei where surface and sub-saturation densities carry more weight, this absorption is no longer guaranteed to remain accurate, especially in RMF-CC, where the scalar potential is strongly constrained by chiral symmetry and therefore has less phenomenological flexibility.

For PDM-3, the unconstrained higher-order terms in the scalar-field potential may also provide additional flexibility in reproducing light nuclei through the fitting procedure, although a more detailed discussion is given in [31].

We can similarly look at the charge density profile in Fig. 5, which is obtained after convoluting the proton density of Eq. (9) with the proton form factor [35]. We can see it exhibits the same plateau behavior as we go from light to heavy nuclei, again reflecting the increasing importance of bulk properties in heavier nuclei. For ^{16}O and ^{48}Ca , the central density is reduced compared to other models, while the surface density is enhanced, shifting the charge outward and increasing the charge radius, as seen in Fig. 3. So RMF-CC1 exhibits a more diffuse charge density profile.

For the charge radii, the results between different models are quite similar, with less than $\sim 2\%$ deviation from experimental values, as seen in Figure 3.

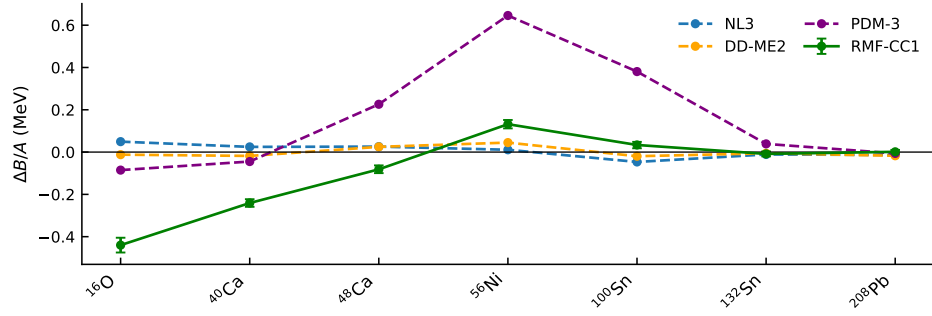


FIG. 2. Deviation of the theoretical binding energy per nucleon $\Delta B/A$ (MeV) from the experimental values of Table III, using the parameterizations in Table IV, for the RMF-CC1, NL3, DD-ME2 and PDM-3 models.

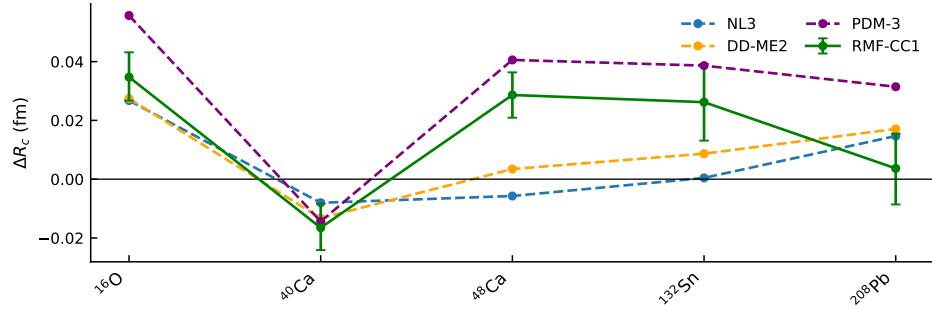


FIG. 3. Deviation of the theoretical charge radii ΔR_c (fm) from the experimental values of Table III, using the parameterizations in Table IV, for the RMF-CC1, NL3, DD-ME2 and PDM-3 models.

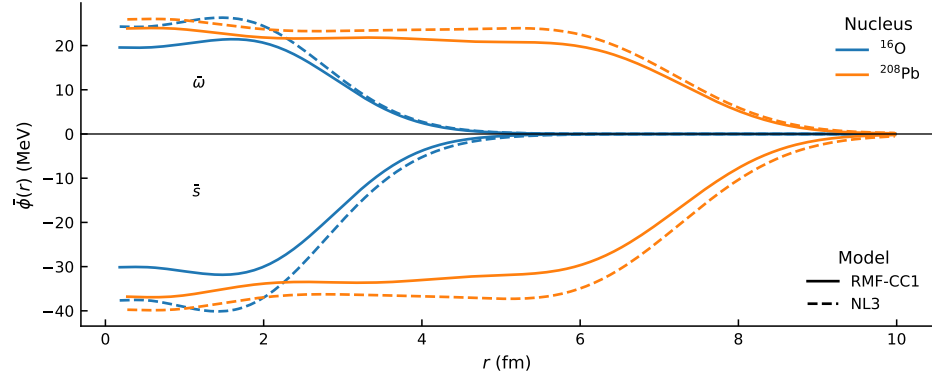


FIG. 4. Mean field profile of the scalar field $\bar{s}(r)$ and vector field $\bar{\omega}(r)$ as a function of the radius. We compare the profiles of a light nucleus ^{16}O and a heavy one ^{208}Pb for both RMF-CC1 and NL3 models.

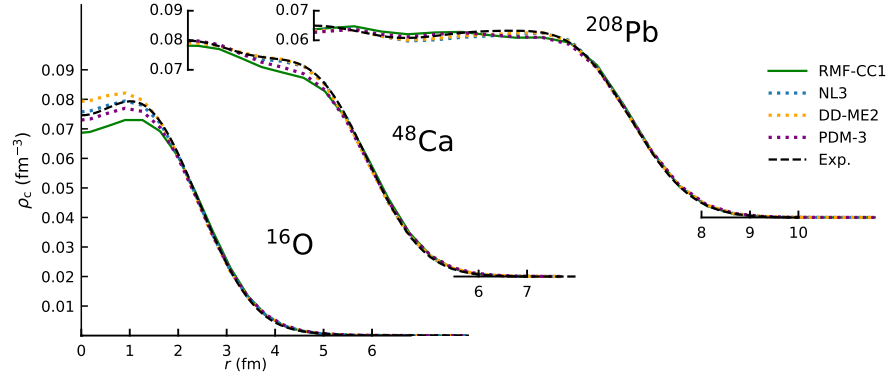


FIG. 5. Comparison of the charge density profile as a function of the radius, for the light ^{16}O , medium ^{48}Ca and the heavy ^{208}Pb nuclei, for the three models RMF-CC1, NL3, DD-ME2 and PDM-3 and experimental data from [36].

B. Open-shell nuclei

In this section, we consider the RMF-CC1 parameter set obtained from the fit to doubly magic nuclei and NEPs in Sec. IV A and Table IV, and we explore open-shell nuclei with a pairing interaction which is a Gogny type separable interaction based on the Gogny force D1S [37] rendering the computation easier [24]. So far this pairing was turned off since we were considering closed shells only.

We observe a good description of heavy nuclei from RMF-CC1, while light and some intermediate mass nuclei are not well described, as previously observed. The surprising part is the appearance of anomalous pairing in the case of the doubly magic nuclei previously studied for RMF-CC1. This is even more pronounced for the PDM-3. The pairing correlations from the separable Gogny force are not automatically zero for closed shells, in fact if the gap around the Fermi level is low enough, we could still have nonzero pairing. The higher Dirac/NR effective mass in RMF-CC1 and PDM-3 compared to NL3 or DD-ME2, seen from Table V, leads to a higher density of states around the Fermi level, which explains why we might have this anomaly. Reducing the pairing strength for both protons and neutrons by ~ 0.9 , is enough to remove this effect using the parametrization of Table IV for RMF-CC1. However, PDM-3 remains largely anomalous and it had to be rescaled by 0.4 in order to remove the anomalous pairing. The obtained results, after applying this reduced pairing strength, are shown in Figure 6.

We obtain a similar conclusion as before concerning the binding energies; the first couple of light nuclei have a stronger deviation from experiments for RMF-CC1, however, for intermediate mass to heavy nuclei, we have excellent agreement. The charge radii are still within $\sim 2\%$ deviation from the experimental values. We notice that even though the anomalous pairing is gone for the specific parameterization we considered from Table IV after pairing strength reduction, posterior samples generated by the MCMC procedure still include parameterizations for which this anomaly persists, as can be seen from the error bars around the pairing energy for the closed neutron shell of ^{48}Ca , or the closed proton shell of ^{214}Pb . In the PDM-3 case, with a NR effective mass of $M_{NR}^* = 0.89M_N$, the anomaly is strongly suppressed by the strong reduction of the pairing strength, it is even zero for the open proton shell in ^{90}Zr . Of course, this is a simplified pairing interaction, where the main focus is on structure properties like the binding energy and charge radius, where the effect of pairing energy is supposed to be negligible. The reduction of the pairing strength is more of a diagnostic treatment of pairing behavior, while a more systematic study is beyond the current scope of this work. For a spectroscopic study, a more careful treatment of pairing should be considered, for example, by refitting the pairing strength to some single-particle energy gaps.

In Figure 7, we show the single particle energies (SPE) for the ^{48}Ca nucleus, for both neutrons and protons. This nucleus was the first doubly magic nucleus to present an anomalous pairing, if not for the reduction of the pairing strength, and it was present in the neutron shell. The link to both Dirac masses and NR masses can now be clarified. This is directly visible in the $1p_{3/2}$ - $1p_{1/2}$ and $1d_{5/2}$ - $1d_{3/2}$ doublets, and is quantified in Table VI for the neutron SPE shell structure. For instance, the p -splitting decreases from about 3.2-3.3 MeV in DD-ME2/NL3 to 2.04 MeV in RMF-CC1 and 0.67 MeV in PDM-3, while the d -splitting is reduced from about 6.2 MeV to 3.82 MeV and 1.28 MeV, respectively. This reduced splitting is consistent with a weaker effective spin-orbit interaction, which mechanically leads to a compression of the shell structure around the Fermi energy. Consistently, the $N = 28$ gap is also reduced, from about 5 MeV in DD-ME2/NL3 to 4.36 MeV in RMF-CC1 and as low as 1.75 MeV in PDM-3, indicating a much softer shell closure.

A second observation is the modification of the level ordering above the Fermi energy. As shown in Table VI, RMF-CC1 and PDM-3 exhibit a negative value of $\Delta_{fp} = \epsilon(1f_{5/2}) - \epsilon(2p_{1/2})$, corresponding to an inversion of the $2p_{1/2}$ and $1f_{5/2}$ states compared to DD-ME2 and NL3. Since $1f_{5/2}$ has a larger degeneracy, bringing it closer to the Fermi energy increases the effective level density in its vicinity, which enhances pairing correlations.

Taken together, the reduced spin-orbit splittings, the smaller $N = 28$ gap, and the modified $2p$ - $1f$ ordering indicate a compressed spectrum and an increased density of states around the Fermi energy in RMF-CC1 and PDM-3. These features correlate with the onset of anomalous pairing observed in the neutron shell of ^{48}Ca .

These differences can be traced back to the larger effective masses obtained in RMF-CC1 and PDM-3, which are associated with their underlying Lagrangian structure (chiral potential + nucleon polarization). Larger values of the Dirac and NR effective masses lead to a denser single-particle spectrum and a reduced spin-orbit splitting, consistently implying stronger pairing.

To finally conclude this discussion, we choose to represent the neutron's spin-orbit potential $V_{\text{so}}(r)$ for ^{48}Ca (we represent $rV_{\text{so}}(r)$ to factor out the $1/r$ dependence in Eq. (19)). The formula is taken from [38] and given by

$$V_{\text{so}}(r) = \frac{1}{2r} \frac{d}{dr} (\Sigma_0(r) - \Sigma_S(r)), \quad (19)$$

with

$$\mathcal{M}(r) = M_N + \frac{1}{2} (\Sigma_S(r) - \Sigma_0(r)) = M_D^*(r) - \frac{1}{2} (\Sigma_S(r) + \Sigma_0(r)). \quad (20)$$

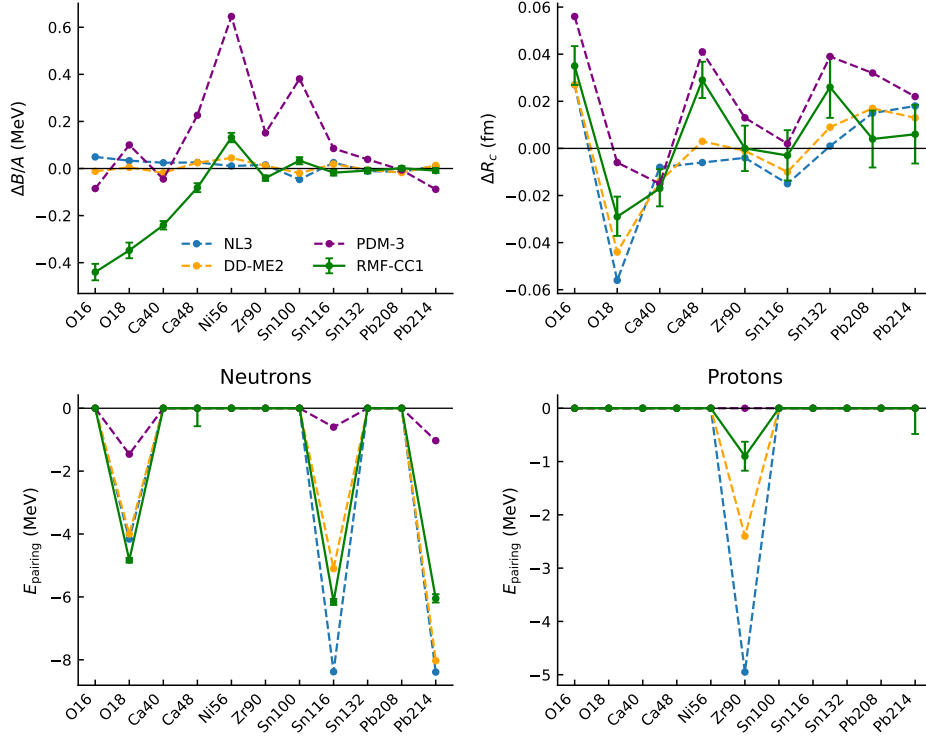


FIG. 6. Deviation of the theoretical binding energy per nucleon $\Delta B/A$ (MeV) and charge radii from the experimental values in [25, 26] (top panels), and comparison of pairing energies for neutrons/protons (bottom panels) using the parameterizations in Table IV, for the RMF-CC1, NL3, DD-ME2 and PDM-3 models, with a separable Gogny force for the pairing interaction, after the reduction of the pairing strength.

The plot is shown in Fig. 8, for the 4 models, and it is fully consistent with our previous discussion. We notice that the spin-orbit strength is much weaker for RMF-CC1 and PDM-3, and the profile is much more diffuse, especially near the surface region at $r \sim 3.2$ fm, which is exactly what compresses the splitting of the spin-orbit doublets and leads to a higher density of states around the Fermi level.

A natural question raised by these results is why the RMF-CC1 model, which provides a satisfactory description of nuclear matter properties and bulk observables, exhibits a shell structure which is not supported by nuclear experimental data, in particular through a reduced spin-orbit splitting. This apparent tension reflects the fact that nuclear matter and finite nuclei probe different aspects of the underlying functional.

In nuclear matter, the constraints primarily fix the behavior of the model in a uniform medium, namely combinations of scalar and vector self-energies at a given density. In contrast, the spin-orbit interaction in finite nuclei is governed by the spatial structure of these fields, in particular their radial dependence in the surface region and the gradients of specific combinations of scalar and vector potentials. These quantities are not constrained by nuclear matter properties.

From this perspective, the reduced spin-orbit splittings, the compression of the single-particle spectrum, and the weakening of the $N=28$ shell gap observed in RMF-CC1 and PDM-3 can be interpreted as signatures of an effective spin-orbit potential that is too weak and/or too diffuse in the surface region, as we have seen in Fig. 8. This naturally leads to a reduction of the gap around the Fermi energy, so a disappearance of magic numbers, and correlates with the appearance of anomalous pairing.

More generally, this behavior highlights a limitation of the RMF-CC framework: the strong constraints imposed by the chiral potential reduce the flexibility of the model to simultaneously reproduce bulk properties and detailed shell structure in finite nuclei. In contrast, phenomenological functionals such as NL3 or DD-ME2 can compensate this through free parameters, be it in the scalar potential (NL3) or in the density dependence of the couplings (DD-ME2).

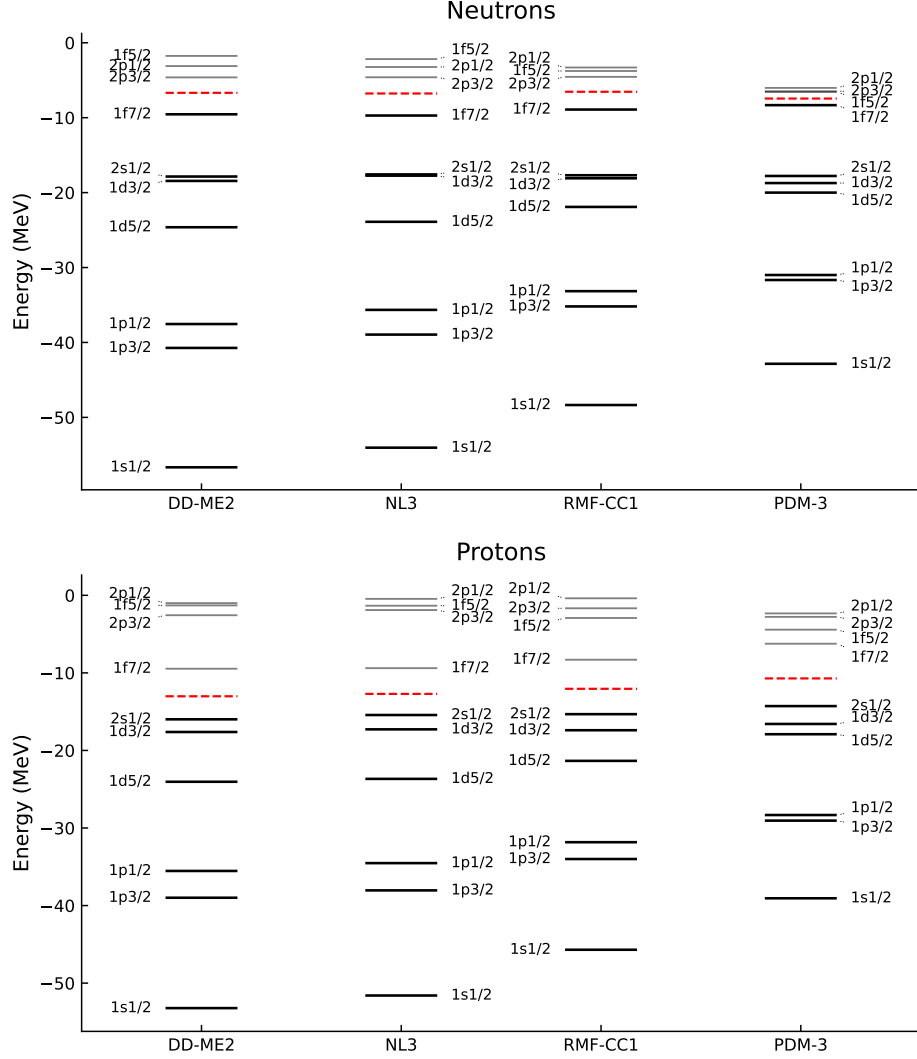


FIG. 7. Comparison of the single particle energies of ^{48}Ca between the various models, and for neutrons (top) and protons (bottom). The red line corresponds to the Fermi energy.

TABLE VI. Neutron single-particle shell structure around the Fermi surface for ^{48}Ca . The Fermi gap Δ_F indicates the energy gap between the first unoccupied and the last occupied levels. $\Delta_p = \epsilon(1p_{1/2}) - \epsilon(1p_{3/2})$ and $\Delta_d = \epsilon(1d_{3/2}) - \epsilon(1d_{5/2})$ denote spin-orbit splittings. $\Delta_{fp} = \epsilon(1f_{5/2}) - \epsilon(2p_{1/2})$ indicates the relative ordering of the $1f_{5/2}$ and $2p_{1/2}$ levels (negative values correspond to inversion). All energies are in MeV.

Quantity	DD-ME2	NL3	RMF-CC1	PDM-3
Δ_F	$1f_{7/2} \rightarrow 2p_{3/2}$ (4.93)	$1f_{7/2} \rightarrow 2p_{3/2}$ (5.11)	$1f_{7/2} \rightarrow 2p_{3/2}$ (4.36)	$1f_{7/2} \rightarrow 1f_{5/2}$ (1.75)
Δ_p	3.19	3.30	2.04	0.67
Δ_d	6.18	6.16	3.82	1.28
Δ_{fp}	+1.35	+1.06	-0.47	-0.55

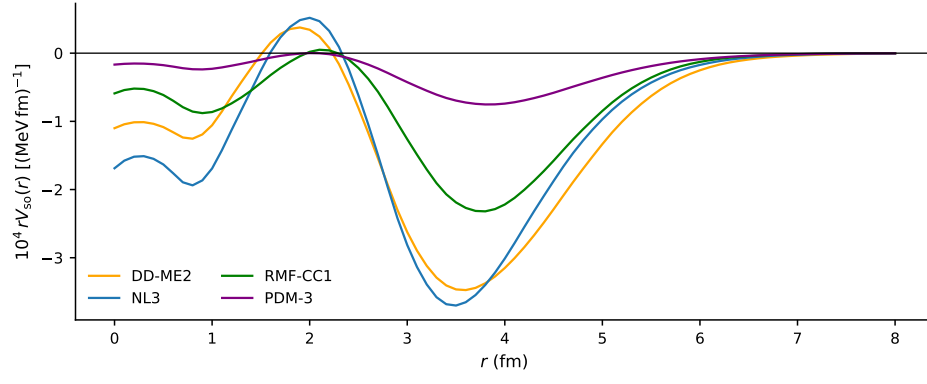


FIG. 8. Comparison of the radial dependence of the spin-orbit strength for neutrons in ^{48}Ca for the DD-ME2, NL3, RMF-CC1 and PDM-3 models. The quantity $rV_{\text{so}}(r)$ is shown to factor out the $1/r$ dependence in the spin-orbit potential $V_{\text{so}}(r)$.

V. SPIN-ORBIT SYSTEMATICS WITHIN THE RMF-CC1 POSTERIOR

In this section, we aim to answer the following question: does the present RMF-CC framework allow one to simultaneously reproduce nuclear matter properties and a realistic spin-orbit strength in finite nuclei, or does it exhibit a structural tension imposed by the constrained form of the model?

More precisely, we want to determine whether the observed weak spin-orbit sector is due to a poor choice of parameters, or whether it reflects a limitation of the RMF-CC predictions, in which the same constrained degrees of freedom control both bulk properties and the spin-orbit behavior.

To answer this, we need to analyze the posterior distribution rather than individual parameterizations, and test whether there exist regions of the posterior that reconcile both nuclear matter constraints and spin-orbit properties.

We first identify a set of spin-orbit diagnostics and examine their correlations with the NEPs. Several quantities were computed: the p - and d -doublet splittings, denoted by Δ_p and Δ_d , the gap around the Fermi energy Δ_F , the maximum of the spin-orbit potential (19), represented by the quantity $\max |rV_{\text{so}}|$, and the integral measure $\int r^2 |V_{\text{so}}| dr$. Since all these diagnostics display the same qualitative trends, we restrict the discussion to two representative quantities:

- the maximum spin-orbit strength $\max |rV_{\text{so}}|$,
- the p -doublet splitting $\Delta_p = \epsilon(1p_{1/2}) - \epsilon(1p_{3/2})$.

The global correlations are shown in Fig. 9, where the nuclear matter properties n_{sat} , E_{sat} , E_{sym} , K_{sat} , and the Dirac mass M_D^* are plotted together with these two spin-orbit diagnostics.

A clear anti-correlation is observed between the Dirac mass and the spin-orbit diagnostics. However, this mass is also strongly anti-correlated with K_{sat} ; thus, lower values of K_{sat} are associated with larger $\max |rV_{\text{so}}|$ and larger Δ_p . In the present RMF-CC framework, the spin-orbit potential, Dirac mass and the incompressibility K_{sat} are all controlled by the scalar channel, so it is expected that they are correlated.

Now to explore whether there exists some good choice of parametrization to remedy the tension between NEPs and the spin-orbit sector, we plot in Fig. 10 the spin-orbit diagnostics against the nuclear matter properties, with each point colored according to its relative posterior quality,

$$q = \frac{\ell_p - \ell_p^{\min}}{\ell_p^{\max} - \ell_p^{\min}}, \quad (21)$$

where ℓ_p denotes the log-posterior value associated with a given parametrization, so that $q = 1$ corresponds to the best posterior points.

The best posterior points remain in the bulk of the distribution, rather than moving toward the largest spin-orbit values. This indicates that increasing the spin-orbit strength within the present RMF-CC1 model requires moving away from the parameter region favored by the posterior.

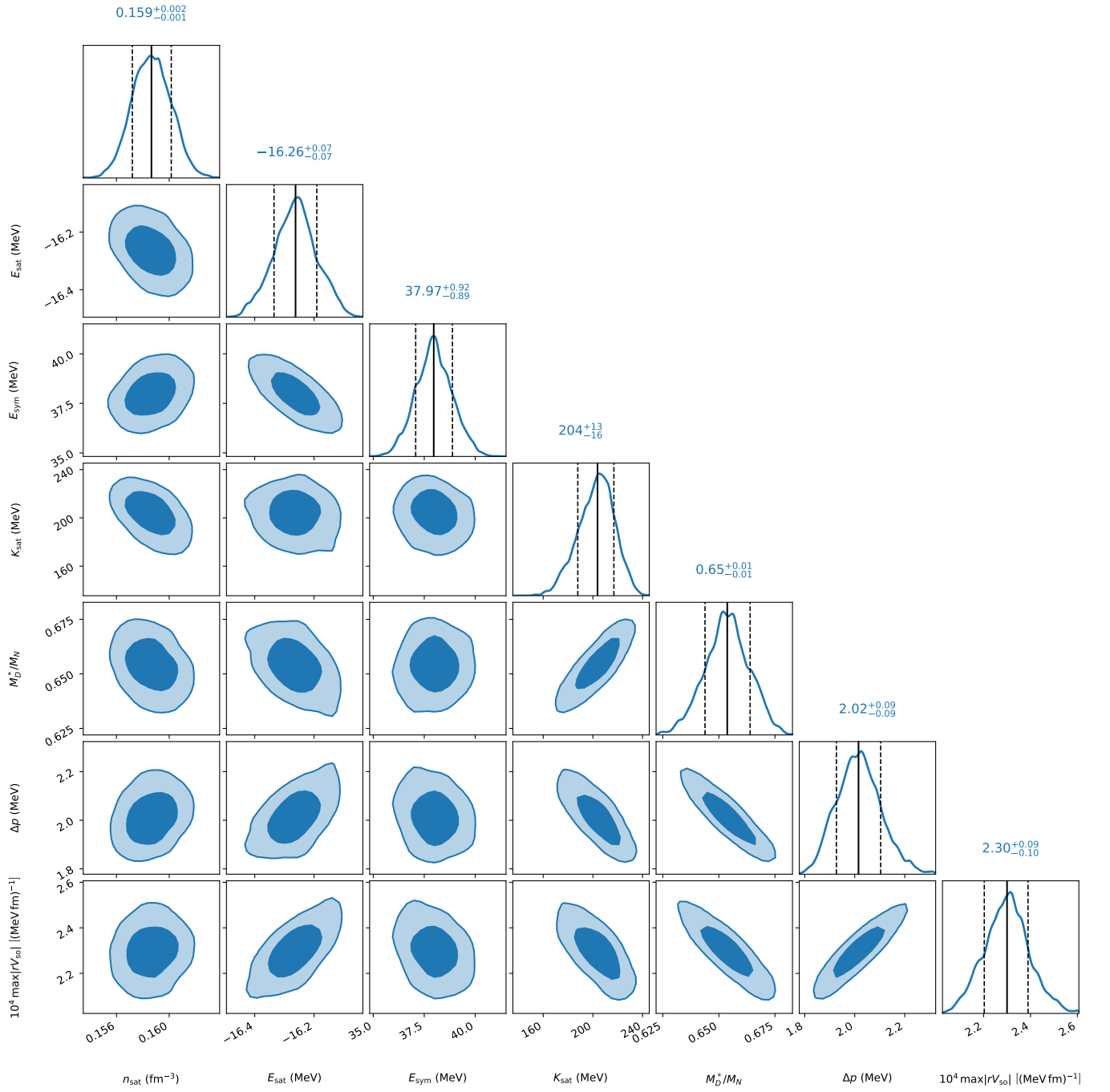


FIG. 9. Corner plot showing the joint and marginalized posterior distributions for the nuclear matter properties n_{sat} , E_{sat} , E_{sym} , K_{sat} , the Dirac mass M_D^*/M_N , and the spin-orbit diagnostics Δ_p and $\max|rV_{\text{so}}|$. The posterior is obtained from the RMF-CC1 model fitted to the data of Tables II and III.

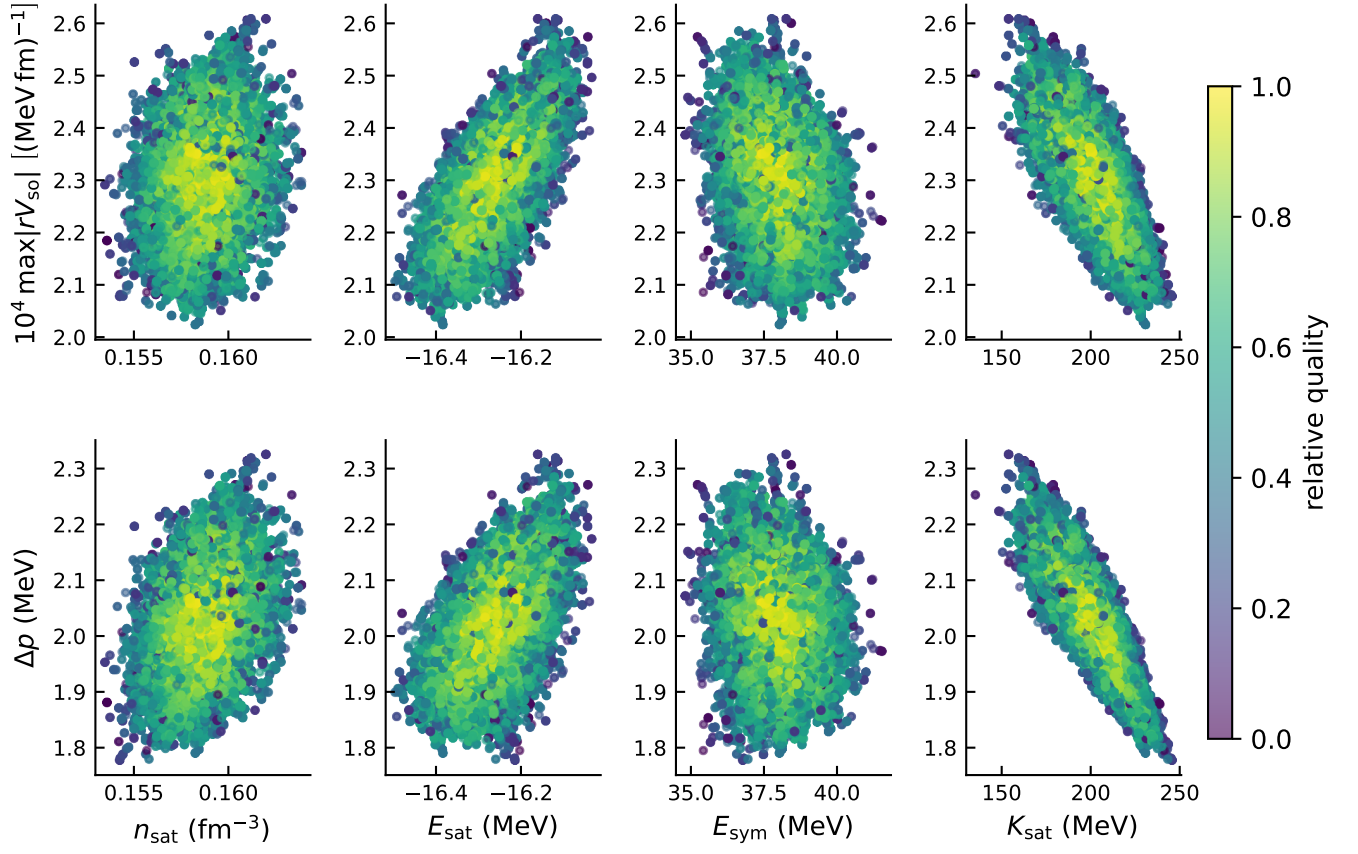


FIG. 10. Correlations between nuclear matter properties and the spin-orbit observables $\max|rV_{so}|$ and Δp . Each point corresponds to a posterior sample and is colored according to its relative posterior quality.

Diagnostic	RMF-CC1 (max)	RMF-CC1 (95%)	DD-ME2	NL3
$10^4 \max rV_{\text{so}} \text{ (MeV fm)}^{-1}$	2.31	2.29	3.47	3.70
$\Delta p \text{ (MeV)}$	2.01	1.99	3.19	3.30

TABLE VII. Maximum and 95th percentile of the spin-orbit observables within the top 10% posterior and the window $K_{\text{sat}} \in [210, 250]$ MeV, compared to DD-ME2 and NL3.

A. Achievable spin-orbit strength within the posterior

To quantify the previous statement, we restrict the posterior sample to:

- the top 10% of points in posterior quality,
- an incompressibility window $K_{\text{sat}} \in [210, 250]$ MeV.

Within this subset, we extract for each spin-orbit diagnostic both the maximum value and the 95th percentile. The latter provides a more robust estimate of what is achievable without relying on extreme outliers. The results are compared to DD-ME2 and NL3 in Table VII.

Two points are important. First, the maximum and the 95th percentile are very close, showing that there is no hidden posterior tail in which the spin-orbit strength is significantly higher. Second, even the largest values remain about 30–40% below DD-ME2 and NL3. This favors the interpretation of a structural limitation of the present RMF-CC1 predictions, rather than a simple poor choice of parameter set.

B. Origin of the weak spin-orbit

To better understand the mechanism behind the reduced spin-orbit strength observed with RMF-CC1, and to determine whether it only originates from the increased effective mass or from surface effects, we decompose the spin-orbit potential in Eq. (19) as

$$rV_{\text{so}}(r) = A(r)B(r), \quad (22)$$

with

$$A(r) = \frac{d}{dr}(\Sigma_0 - \Sigma_S), \quad B(r) = \frac{1}{2\mathcal{M}^2(r)}. \quad (23)$$

Thus, $A(r)$ measures the surface derivative of $\Sigma_0 - \Sigma_S$, while $B(r)$ contains the effective-mass denominator.

We evaluate A and B at the radius r^* where $|rV_{\text{so}}|$ is maximal in the surface region. For RMF-CC1, three representative points are selected from the full posterior distribution, corresponding to the 10th, 50th, and 90th percentiles of K_{sat} . The same decomposition is performed for DD-ME2 and NL3 using the identical definition of r^* . The results are shown in Table VIII.

As discussed before, decreasing K_{sat} within the RMF-CC approach increases the spin-orbit strength. This variation is mainly driven by the surface term $|A(r^*)|$; as we move from the high to low K_{sat} value, $|A(r^*)|$ increases by about 6%, whereas $B(r^*)$ increases by about 3%. By looking at the variation of $\max |rV_{\text{so}}|$, $|A(r^*)|$ makes up around $\sim 70\%$ of its variation. Thus, the variation of the spin-orbit strength is mostly governed by the surface derivative of $V - S$.

The comparison with DD-ME2 and NL3 clarifies the origin of the reduced spin-orbit strength. RMF-CC1 exhibits a smaller surface derivative than both DD-ME2 and NL3, and its effective mass factor $B(r^*)$ is also lower. As a result, the suppression of the spin-orbit strength cannot be attributed to a single mechanism. We saw that within the RMF-CC1 posterior, the variation is mainly driven by the surface term $A(r^*)$. However, when compared to standard covariant EDFs, both contributions play a role. Relative to DD-ME2, the difference is indeed dominated by the effective mass factor, whereas for NL3 the surface and effective mass contributions are of similar importance. Overall, the reduced spin-orbit strength reflects the combined effect of a weaker surface derivative and a smaller effective mass factor.

Overall, these results suggest that the constrained scalar sector of the present RMF-CC model ties together the bulk curvature around saturation, the Dirac mass, and the surface derivative of $\Sigma_0 - \Sigma_S$ more strongly than in the typical phenomenological covariant EDFs. This strong constraint, and the inability to reproduce the spin-orbit strength typical of standard covariant EDFs within an acceptable K_{sat} window points towards a missing surface/spin-orbit degree of freedom rather than to a mere readjustment of the nuclear-matter parameters.

Model	K_{sat} (MeV)	r^* (fm)	$ A(r^*) $ (MeV fm $^{-1}$)	$B(r^*)$ (MeV $^{-2}$)	$10^4 \max rV_{\text{so}} $ (MeV fm) $^{-1}$
RMF-CC1 (low K_{sat})	183	3.8	2.74×10^2	8.70×10^{-7}	2.39
RMF-CC1 (mid K_{sat})	204	3.8	2.61×10^2	8.53×10^{-7}	2.23
RMF-CC1 (high K_{sat})	220	3.8	2.58×10^2	8.46×10^{-7}	2.18
DD-ME2	251	3.6	3.06×10^2	1.14×10^{-6}	3.47
NL3	272	3.5	3.36×10^2	1.10×10^{-6}	3.70

TABLE VIII. Decomposition of the spin-orbit potential into the surface factor $A(r) = d(\Sigma_0 - \Sigma_S)/dr$ and the effective-mass factor $B(r) = 1/(2\mathcal{M}^2(r))$, evaluated at the radius r^* where $|rV_{\text{so}}|$ is maximal.

A natural way to restore this flexibility, which was considered in Ref. [39], would be to introduce an additional degree of freedom that is weakly constrained in uniform matter but active in finite nuclei, such as the ω tensor coupling, which is zero in infinite matter but directly modifies the spin-orbit in finite nuclei via the gradients of the ω field. Or, more microscopically, we can consider contributions beyond the Hartree level. In particular, the ρ tensor channel can significantly enhance the spin-orbit strength, as discussed in Ref. [40], and also reduce the Dirac and NR effective masses as shown in Ref. [9].

VI. DEPARTING FROM THE LINEAR SIGMA MODEL

In this last section, we discuss the role of the scalar potential in our results. So far, we considered the $L\sigma M$ for our chiral potential (4). This potential's cubic and quartic terms are fixed by chiral symmetry as mentioned before, however we can allow for a small departure from this fixed value to see its effect on the NEPs and finite nuclei properties. Phenomenologically, this can be motivated by models such as the NJL model, where one can generate a chiral potential based on a more accurate description of the low-energy realization of chiral symmetry breaking in the hadronic sector (see Refs. [10, 15, 41]). As discussed in Ref. [10, 41], linearization of the NJL potential near saturation recovers the $L\sigma M$ but modifies the cubic and quartic coefficients. The scalar potential can be expressed as

$$V_{\chi, \text{NJL}}(s) \approx \frac{1}{2} m_s^2 s^2 + \frac{1}{2} \frac{m_s^2 - m_\pi^2}{f_\pi} (1 - C_{\chi, \text{NJL}}) s^3 + \frac{1}{8} \frac{m_s^2 - m_\pi^2}{f_\pi^2} (1 - 6 C_{\chi, \text{NJL}} + D_{\chi, \text{NJL}}) s^4 + \dots, \quad (24)$$

where $C_{\chi, \text{NJL}}$ and $D_{\chi, \text{NJL}}$ are related to NJL loop integrals [10, 41]. We see that for $C_{\chi, \text{NJL}} = D_{\chi, \text{NJL}} = 0$ we simply recover the $L\sigma M$, while choosing $C_{\chi, \text{NJL}} = 1$ quenches the cubic term, as in the case of the QMC model [12, 42]. These parameters have ranges $C_{\chi, \text{NJL}} \in [0, 1]$ and $D_{\chi, \text{NJL}} \in [0, 5]$. We will thus repeat our previous fitting procedure in Section III while allowing the cubic and quartic coefficients to vary in their respective intervals by imposing it as a prior. Technically, these 2 parameters depend on the same underlying set of hadronic parameters, and so are not independent, but for the sake of this qualitative study, we will treat them as such. The new parametrization is given in Table IX.

We present first the NEP results in Table X. We observe a slight lowering of the symmetry energy, while the incompressibility modulus is now within expected experimental window. However, the main point is the Dirac and NR effective masses, which are now lowered down to $0.58M_N$ and $0.66M_N$ respectively. This is expected to enhance the spin-orbit strength and open the shell gaps around the Fermi surface, and the previously observed pairing anomaly should vanish. Indeed, results in Figure 11, show an improvement of the predictions for the binding energy and charge radii for intermediate and low mass nuclei. In addition, the pairing anomaly also disappears. This is detected by the fact that all parameterizations within the 68% CI for the NJL potential give zero pairing at closed shells, unlike the $L\sigma M$ ones, where we still observed some small but non-zero pairing for ^{48}Ca (neutrons) and ^{214}Pb (protons). This confirms our previous justification about the importance of the potential for light nuclei: by relaxing the strongly constrained chiral potential, we are able to better reproduce the properties of light and intermediate mass nuclei. Of course, this relaxation comes with 2 new parameters to fit, similarly to NL3. However, these 2 parameters are constrained to remain close to their value imposed by the NJL model. This also confirms the role of the Dirac and NR effective masses in the shell structure. This is, however, a qualitative result; it allows us to better understand the role of the chiral potential and the Dirac mass emerging from RMF-CC and PDM-3. The former seems to affect light nuclei, and the latter strongly affects the shell structure. However, in the present work, $C_{\chi, \text{NJL}}$ and $D_{\chi, \text{NJL}}$ are treated as independent phenomenological parameters to test the sensitivity of finite nuclei to the stiffness of the scalar potential. This should not be interpreted as a fully consistent NJL matching, where these coefficients are correlated by the underlying loop integrals. A real study of the NJL potential requires performing the same approach as in the works of Refs. [10, 41], which is beyond the current scope of this work.

TABLE IX. Model parameters for RMF-CC maximising the posterior probability for the FN data and the NEPs, for the $L\sigma M$ and NJL potentials.

Parameter	$L\sigma M$	NJL
m_s (MeV)	659.474	564.225
g_s	11.9268	11.3178
g_ω	11.3726	12.9789
g_ρ	4.4302	4.2592
C_{NS}	0.8064	0.2537
$C_{\chi,NJL}$	0	0.9588
$D_{\chi,NJL}$	0	3.4985

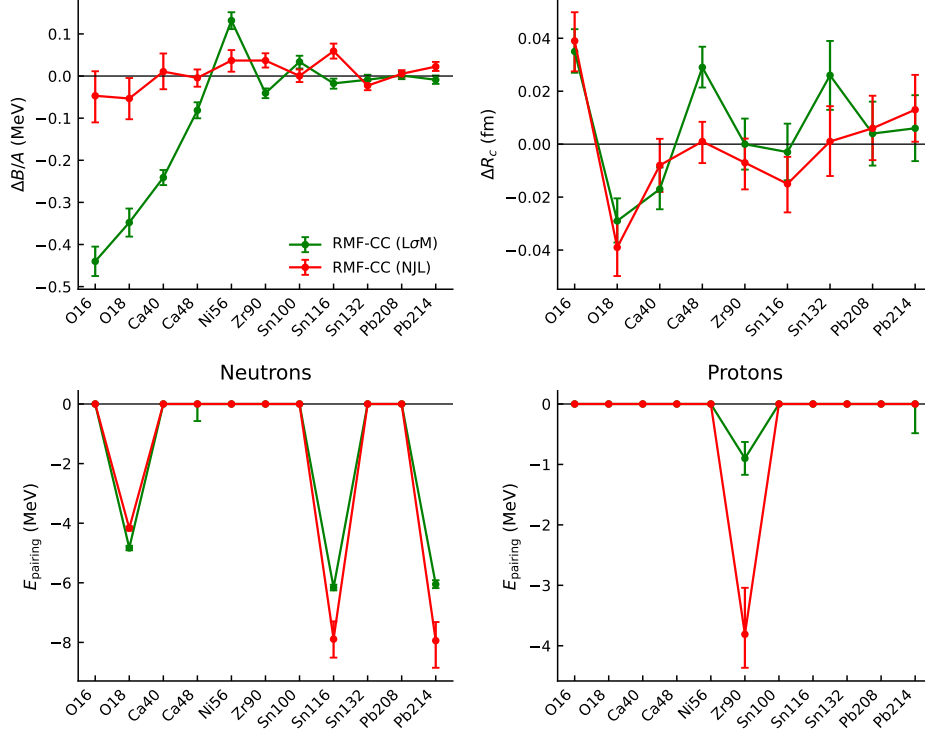


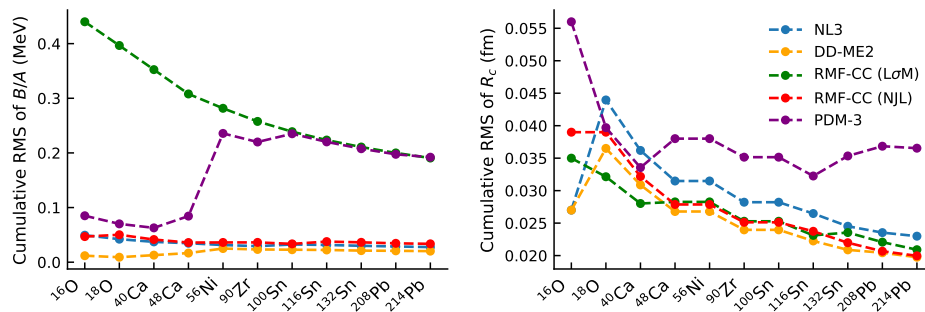
FIG. 11. Deviation of the theoretical binding energy per nucleon $\Delta B/A$ (MeV) and charge radii from the experimental values from Refs.[25, 26] (top panels), and pairing energies comparison for neutrons/protons (bottom panels) using the parameterizations in Table IX, for the RMF-CC with $L\sigma M$ and NJL potentials, with a separable Gogny force for the pairing interaction, after the reduction of the pairing strength.

Finally, Figure 12 shows the cumulative root mean square (rms) for the various models for B/A and R_c , which allows us to have a test on the predictions of these various models as we move from lighter to heavier nuclei. As discussed in Section IV, the RMF-CC model with the $L\sigma M$ predictions improved when moving towards heavier nuclei. This trend can be seen as the rms gets smaller and smaller, reaching ~ 0.2 MeV. The PDM-3 model tends to the same final rms, however, the trend is that its predictions are degraded when we move to heavier nuclei. This rms is, however, one order of magnitude larger than the other models (NL3, DD-ME2), while the RMF-CC (NJL) predictions are on par with them, with an rms of ~ 0.03 MeV.

In the case of charge radii, the RMF-CC model performs quite well with both versions of the potential, with a final rms of ~ 0.02 fm, an even better rms than that of the NL3 model.

TABLE X. The reproduced NEPs using the parametrization of Table IX. We show both the $L\sigma M$ and the NJL predictions.

Parameters	$L\sigma M$	NJL
E_{sat} (MeV)	-16.26	-16.10
n_{sat} (fm^{-3})	0.159	0.152
E_{sym} (MeV)	38	36.98
K_{sat} (MeV)	199	234
M_D^*/M_N	0.65	0.58
M_{NR}^*/M_N	0.72	0.66

FIG. 12. The cumulative root mean square for the various models considered in this work for the binding energy per nucleon B/A (MeV) and the charge radius R_c (fm).

VII. CONCLUSIONS

In this work, we have considered an RMF framework supplemented with a chiral potential and confinement effects, which was previously applied to nuclear matter [7–10]. It has been extended to the description of finite spherical nuclei at the Hartree approximation for the first time. The parameters of the model are adjusted to reproduce both NEPs at saturation and finite nuclei properties, such as binding energies and charge radii of doubly magic nuclei, and give the RMF-CC1 parametrization. The resulting functional provides a consistent description of bulk nuclear properties while being a QCD-motivated covariant EDF: its scalar sector is constrained by chiral symmetry breaking through the identification of the scalar field with the chiral-invariant field associated with the radial fluctuation of the chiral condensate, while confinement-inspired nucleon response is encoded through a scalar polarizability introduced in Ref. [6] and associated with the self-consistent readjustment of the quark wave functions as originally proposed in Ref. [12]. The resulting parametrization provides a consistent description of bulk nuclear properties, while satisfying QCD-motivated constraints: the chiral potential is fixed and the identification of the scalar field with the chiral-invariant field associated with the radial fluctuation of the chiral condensate, and the inclusion of the nucleon response motivated by Ref. [12].

For doubly magic nuclei, we observed that the RMF-CC1 reproduces the binding energies and charge radii reasonably well within the considered uncertainties. The charge radii remain close to experiment, with less than 2% deviation from experimental values, and comparable in quality to NL3 and DD-ME2, while the binding energies showed a more interesting trend: the largest deviations ($\sim 5\%$), occur for light nuclei, whereas the agreement improves significantly from medium to heavy nuclei. To understand the role of the scalar potential, we focused our attention on the RMF-CC1 and NL3 models, which share a non-linear potential, where the NL3 potential, however, is not constrained by chiral symmetry breaking. By looking at the scalar field profile inside the nucleus, we saw that the scalar field has a large plateau for heavier nuclei, so the system probes the scalar potential mostly around the saturation value, where both RMF-CC1 and NL3 potentials are fitted to behave similarly. However, for light nuclei, a broader interval of the potential is probed within the nuclear radius, making them more sensitive to the global shape of the scalar potential away from saturation. Since the RMF-CC potential is strongly constrained by chiral symmetry, it is less flexible than the phenomenological NL3 potential, whose nonlinear coefficients are adjusted directly to finite nucleus data. This naturally explains why NL3 performs better for light nuclei, whereas RMF-CC1 becomes more accurate for heavier

systems, dominated by bulk properties.

We then proceeded to study open-shell nuclei, equipped with a separable Gogny-type pairing interaction. We found that for the pairing strength considered for the force D1S [37], RMF-CC1 and PDM-3 exhibit an anomalous pairing in some closed shell nuclei. This effect can be traced to the larger Dirac and NR effective masses predicted by these 2 classes of models, which reduce spin-orbit splittings and compress the single-particle spectrum around the Fermi surface and thus enhance pairing. A modest reduction of the pairing strength suppresses this anomaly at the diagnostic level for RMF-CC1, which had a Dirac (NR) effective mass of $0.65M_N$ ($0.72M_N$), and gives a reasonable description of both closed and open shell nuclei. However, it was not enough for the PDM-3 with a Dirac (NR) effective mass of $0.83M_N$ ($0.89M_N$), which required a drastic reduction in the pairing strength. We observe overall good agreement for medium and heavy nuclei, while again the RMF-CC1 has larger deviations compared to the NL3 and DD-ME2 models. To observe the effect of these effective masses, we looked at the SPE of the ^{48}Ca , and observed both a reduction in the spin-orbit splitting, linked to the large Dirac mass, which also changes the ordering of some energy levels above the Fermi level ($2p1/2$ and $1f5/2$) compared to NL3 and DD-ME2, and a reduction of the shell gaps around the Fermi level. Both of these effects can explain the observation of an enhanced and sometimes anomalous pairing. We also checked the spin-orbit potential and indeed confirmed that it is much weaker and more diffuse for RMF-CC1 and PDM-3 with the large Dirac effective masses, again reinforcing the link with the weak spin-orbit splitting and the higher density of states around the Fermi level.

A systematic study was then done to answer two questions: do there exist within our RMF-CC1 phase space, parameterizations that are able to remedy the weak spin-orbit potential while respecting NEPs, and whether the major reduction of the spin-orbit potential is due to surface effects or merely the large effective mass. We managed to show that even the largest spin-orbit magnitudes reached are still 30-40% lower than typical covariant EDFs such as DD-ME2 and NL3. Additionally, we traced back the origin of this deficit to an interplay between surface effects and the large effective mass exhibited by RMF-CC1.

Finally, we allowed for a small deviation away from the $L\sigma M$ to explore the role played by the potential in the RMF-CC model. It supports that the global trend of the potential matters more for light nuclei, while the chiral potential performs very well for medium and heavy nuclei. It also confirms once again that the Dirac and NR effective masses are heavily responsible for the enhanced and thus anomalous pairing that is seen for some parameterizations, at least within the separable Gogny interaction considered here.

Overall, the present results show that RMF-CC constitutes a valid framework for the description of finite nuclei and nuclear matter, while being anchored in QCD aspects such as chiral symmetry breaking and confinement effects via nucleon polarization. However, there is a limitation appearing when considering a more systematic study for pairing and when trying to have a more global fitting procedure: the effective masses are too large, leading to a weak spin-orbit potential, which strongly enhances pairing interaction. The strongly constrained scalar sector of RMF-CC ties together the bulk curvature around saturation, the Dirac mass, and the surface derivative appearing in the spin-orbit potential, and is too rigid to reconcile them without additional field couplings. A qualitative improvement was seen by exploring the NJL inspired scalar potential. Therefore, one path would be to consider a more systematic study within this approach.

A related limitation was also observed in the astrophysical sector, where RMF-CC tends to favor a larger slope of the symmetry energy, leading to tensions with astrophysical constraints when the model is calibrated to neutron-star observables [43]. This suggests that additional isovector flexibility may be required. A natural phenomenological extension would be to introduce cross-meson couplings, in particular a vector-isovector coupling, as explored in Ref. [43], and to perform a joint calibration to finite-nucleus observables, nuclear empirical parameters, and astrophysical constraints.

Other natural extensions that could affect the spin-orbit potential include adding, at the Hartree level, a tensor isoscalar term, as in Ref.[39], or, more microscopically, adding the Fock terms. As shown in Ref. [40], the tensor ρ interaction plays an important role in the strength of the spin-orbit potential, and RHF studies for infinite matter, such as in Ref. [9], seem to point to a reduction of the Dirac and NR effective masses when Fock terms are included. A natural next step is therefore to include the Fock terms, and include a systematic refit of the pairing strength to some spectroscopic data. This can provide a valuable extension towards a more complete and accurate energy density functional for finite nuclei and nuclear matter.

Acknowledgments: The authors acknowledge the support of the project RELANSE ANR-23-CE31-0027-01 of the French National Research Agency (ANR), the CNRS-IN2P3 MAC2 masterproject, the European Union's Horizon 2020 research and innovation program under grant agreement STRONG-2020-No824093.

[1] Y. Nambu, G. Jona-Lasinio, Phys. Rev. **124**, 246 (1961). doi:10.1103/PhysRev.124.246

- [2] S. Weinberg, *Phys. Lett. B* **251**, 288 (1990). doi:10.1016/0370-2693(90)90938-3
- [3] P. Ring, *Prog. Part. Nucl. Phys.* **37**, 193 (1996). doi:10.1016/0146-6410(96)00054-3
- [4] D. Vretenar, A. Afanasjev, G. Lalazissis, P. Ring, *Physics Reports* **409**(3), 101 (2005). doi: <https://doi.org/10.1016/j.physrep.2004.10.001>
- [5] J. Meng, H. Toki, S.G. Zhou, S.Q. Zhang, W.H. Long, L.S. Geng, *Progress in Particle and Nuclear Physics* **57**(2), 470 (2006). doi:10.1016/j.pnpnp.2005.06.001
- [6] G. Chanfray, M. Ericson, *Eur. Phys. J. A* **25**, 151 (2005). doi:10.1140/epja/i2005-10074-6
- [7] E. Massot, G. Chanfray, *Phys. Rev. C* **78**, 015204 (2008). doi:10.1103/PhysRevC.78.015204
- [8] R. Somasundaram, J. Margueron, G. Chanfray, H. Hansen, *Eur. Phys. J. A* **58**(5), 84 (2022). doi:10.1140/epja/s10050-022-00733-7
- [9] M. Chamseddine, J. Margueron, G. Chanfray, H. Hansen, R. Somasundaram, *The European Physical Journal A* **59**(8) (2023). doi:10.1140/epja/s10050-023-01089-2. URL <http://dx.doi.org/10.1140/epja/s10050-023-01089-2>
- [10] M. Chamseddine, J. Margueron, H. Hansen, G. Chanfray, *The European Physical Journal A* **60**, 137 (2024). doi: 10.1140/epja/s10050-024-01358-8
- [11] G. Chanfray, M. Ericson, P.A.M. Guichon, *Phys. Rev. C* **63**, 055202 (2001). doi:10.1103/PhysRevC.63.055202
- [12] P.A.M. Guichon, *Phys. Lett. B* **200**, 235 (1988). doi:10.1016/0370-2693(88)90762-9
- [13] G. Chanfray, D. Davesne, M. Ericson, M. Martini, *Eur. Phys. J. A* **27**, 191 (2006). doi:10.1140/epja/i2005-10245-5
- [14] M.C. Birse, *Phys. Rev. C* **53**, R2048 (1996). doi:10.1103/PhysRevC.53.R2048
- [15] G. Chanfray, *Eur. Phys. J. A* **60**(1), 7 (2024). doi:10.1140/epja/s10050-023-01221-2
- [16] G. Chanfray, M. Ericson, *Phys. Rev. C* **75**, 015206 (2007). doi:10.1103/PhysRevC.75.015206
- [17] E. Massot, G. Chanfray, *Phys. Rev. C* **80**, 015202 (2009). doi:10.1103/PhysRevC.80.015202
- [18] G. Chanfray, M. Ericson, *Phys. Rev. C* **83**, 015204 (2011). doi:10.1103/PhysRevC.83.015204
- [19] G. Chanfray, M. Ericson, M. Martini, *Universe* **9**(7) (2023). doi:10.3390/universe9070316. URL <https://www.mdpi.com/2218-1997/9/7/316>
- [20] K. Hebeler, J.M. Lattimer, C.J. Pethick, A. Schwenk, *Astrophys. J.* **773**, 11 (2013). doi:10.1088/0004-637X/773/1/11
- [21] J. Margueron, R. Hoffmann Casali, F. Gulminelli, *Phys. Rev. C* **97**(2), 025805 (2018). doi:10.1103/PhysRevC.97.025805
- [22] J. Margueron, F. Gulminelli, *Physical Review C* **99** (2019). doi:10.1103/PhysRevC.99.025806
- [23] J. Dobaczewski, W. Nazarewicz, P.G. Reinhard, *Journal of Physics G: Nuclear and Particle Physics* **41**(7), 074001 (2014). doi:10.1088/0954-3899/41/7/074001. URL <https://dx.doi.org/10.1088/0954-3899/41/7/074001>
- [24] T. Nikšić, N. Paar, D. Vretenar, P. Ring, *Computer Physics Communications* **185**(6), 1808 (2014). doi: <https://doi.org/10.1016/j.cpc.2014.02.027>. URL <https://www.sciencedirect.com/science/article/pii/S0010465514000836>
- [25] G. Audi, F. Kondev, M. Wang, W. Huang, S. Naimi, *Chinese Physics C* **41**, 030001 (2017). doi:10.1088/1674-1137/41/3/030001
- [26] I. Angeli, K. Marinova, *Atomic Data and Nuclear Data Tables* **99**, 69 (2013). doi:10.1016/j.adt.2011.12.006
- [27] B.V. Carlson, M. Dutra, O. Lourenço, J. Margueron, *Phys. Rev. C* **107**, 035805 (2023). doi:10.1103/PhysRevC.107.035805. URL <https://link.aps.org/doi/10.1103/PhysRevC.107.035805>
- [28] M. Bender, P.H. Heenen, P.G. Reinhard, *Rev. Mod. Phys.* **75**, 121 (2003). doi:10.1103/RevModPhys.75.121. URL <https://link.aps.org/doi/10.1103/RevModPhys.75.121>
- [29] G.A. Lalazissis, J. König, P. Ring, *Phys. Rev. C* **55**, 540 (1997). doi:10.1103/PhysRevC.55.540
- [30] G.A. Lalazissis, T. Nikšić, D. Vretenar, P. Ring, *Phys. Rev. C* **71**, 024312 (2005). doi:10.1103/PhysRevC.71.024312
- [31] M.H. Mun, I.J. Shin, W.G. Paeng, M. Harada, Y. Kim, *Eur. Phys. J. A* **59**(7), 149 (2023). doi:10.1140/epja/s10050-023-01064-x
- [32] M. Jaminon, C. Mahaux, *Phys. Rev. C* **40**, 354 (1989). doi:10.1103/PhysRevC.40.354
- [33] Z.y. Ma, J. Rong, B.Q. Chen, Z.Y. Zhu, H.Q. Song, *Phys. Lett. B* **604**, 170 (2004). doi:10.1016/j.physletb.2004.11.004
- [34] E.N.E.v. Dalen, C. Fuchs, A. Faessler, *Phys. Rev. C* **72**, 065803 (2005). doi:10.1103/PhysRevC.72.065803
- [35] J.M. Yao, S. Baroni, M. Bender, P.H. Heenen, *Phys. Rev. C* **86**, 014310 (2012). doi:10.1103/PhysRevC.86.014310
- [36] H. De Vries, C. De Jager, C. De Vries, *Atomic Data and Nuclear Data Tables* **36**(3), 495 (1987). doi:[https://doi.org/10.1016/0092-640X\(87\)90013-1](https://doi.org/10.1016/0092-640X(87)90013-1). URL <https://www.sciencedirect.com/science/article/pii/0092640X87900131>
- [37] J. Berger, M. Girod, D. Gogny, *Computer Physics Communications* **63**(1), 365 (1991). doi:[https://doi.org/10.1016/0010-4655\(91\)90263-K](https://doi.org/10.1016/0010-4655(91)90263-K). URL <https://www.sciencedirect.com/science/article/pii/001046559190263K>
- [38] J.P. Ebran, A. Mutschler, E. Khan, D. Vretenar, *Phys. Rev. C* **94**, 024304 (2016). doi:10.1103/PhysRevC.94.024304. URL <https://link.aps.org/doi/10.1103/PhysRevC.94.024304>
- [39] F. Mercier, J.P. Ebran, E. Khan, *Phys. Rev. C* **107**, 034309 (2023). doi:10.1103/PhysRevC.107.034309. URL <https://link.aps.org/doi/10.1103/PhysRevC.107.034309>
- [40] G. Chanfray, J. Margueron, *Phys. Rev. C* **102**, 024331 (2020). doi:10.1103/PhysRevC.102.024331. URL <https://link.aps.org/doi/10.1103/PhysRevC.102.024331>
- [41] G. Chanfray, H. Hansen, J. Margueron, *Eur.Phys.J.A* **59**(11), 264 (2023). doi:10.1140/epja/s10050-023-01179-1. URL <https://hal.science/hal-04074564>
- [42] P.A.M. Guichon, A.W. Thomas, *Phys. Rev. Lett.* **93**, 132502 (2004). doi:10.1103/PhysRevLett.93.132502
- [43] B.K. Pradhan, et al., Relativistic mean field approach with chiral symmetry breaking and quark confinement in the light of astrophysical constraints (2026). In Preparation